Geochemical Perspectives Letters

Brucite formation and dissolution in oceanic serpentinite

F. Klein[1*], S.E. Humphris[1], W. Bach[2]

OPEN ACCESS

doi: 10.7185/geochemlet.2035

Abstract

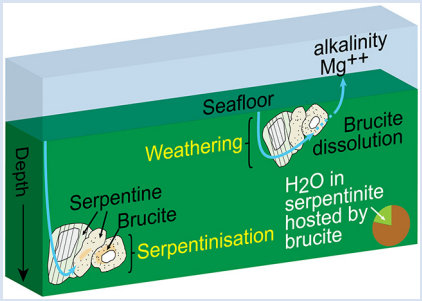

Brucite is an important, albeit elusive, hydrous mineral formed during serpentinisation, a vector of Mg from the mantle to seawater, and possibly a significant host of water in oceanic serpentinite. However, the abundance of brucite has not been quantified in oceanic serpentinite and its fate and related chemical fluxes remain uncertain. We used thermal analysis and confocal Raman spectroscopy to determine the abundance and distribution of brucite in serpentinite recovered by seafloor drilling (n = 48) and dredging (n = 22). Almost all (90 %) of the drilled serpentinite samples contained brucite. The brucite contents increased with increasing extent of serpentinisation and constituted up to 15.6 wt. % of the altered rock. In contrast, dredged serpentinites were devoid of brucite and lost 4.0 wt. % MgO on average, which translates to an estimated average annual flux of 1.3×10^{10} mole Mg and about 2×10^{10} mole alkalinity during seafloor weathering of serpentinite globally. Our data suggest that, on average, brucite stores ~20 % of the water in unweathered serpentinite, making brucite one of the largest water carriers in slow and ultra-slow spreading oceanic lithosphere.

Received 28 July 2020 | Accepted 18 September 2020 | Published 27 October 2020

Introduction

Tectonic exhumation exposes peridotite to aqueous solutions and, because peridotite is unstable in the presence of H_2O over a wide range of temperatures and pressures, it undergoes a series of dissolution-precipitation and redox reactions to form serpentinite. In addition to serpentine, serpentinites commonly contain other minerals in varying proportions, notably brucite, magnetite, talc, chlorite, and tremolite. Brucite is probably one of the most enigmatic minerals formed during serpentinisation. While it is believed to play a central role in modulating $SiO_{2(aq)}$, pH, and the generation of H_2 (Klein *et al.*, 2013), and is inferred to be a major carrier of water into subduction zones (Kawahara *et al.*, 2016; Peters *et al.*, 2020), few studies have detected brucite in oceanic serpentinite (*e.g.*, Bach *et al.*, 2004; Klein *et al.*, 2009). In contrast to seemingly brucite-poor seafloor serpentinite, some continental exposures of serpentinite reveal up to 47 mole % brucite (Hostetler *et al.*, 1966). Indeed, seafloor serpentinites commonly show lower MgO and higher SiO_2 concentrations than their continental counterparts, which Snow and Dick (1995) attributed to dissolution of brucite and incongruent dissolution of olivine during seafloor weathering. Alternatively, Malvoisin (2015) suggested that the generally lower MgO and higher SiO_2 concentrations in seafloor serpentinites are due to the addition of SiO_2 from gabbroic rocks, which would limit or even prevent brucite formation during serpentinisation. These models imply contrasting, large scale mass transfers between the oceanic lithosphere and seawater (Snow and Dick, 1995) and between mafic and ultramafic rocks within the oceanic lithosphere (Malvoisin, 2015). In this study, we examined the abundance of brucite in oceanic serpentinites. We show that brucite is present in serpentinites recovered by drilling, but absent in serpentinites recovered by dredging directly from the seafloor. We then compare the measured and predicted abundances of brucite in serpentinite and discuss the significance of brucite formation and dissolution in serpentinised oceanic basement.

Materials & Methods

We examined 22 partially to completely serpentinised, carbonate-free peridotites recovered by dredging and 48 recovered by scientific seafloor drilling. Samples were collected during cruises to the Mid-Cayman Rise, Southwest Indian Ridge, Gakkel Ridge, South American Antarctic Ridge, Mid-Atlantic Ridge, East Pacific Rise, Iberian Margin, Tyrrhenian Sea, and the Mariana forearc (Supplementary Information Table S-1). A description of these samples is provided elsewhere (Klein *et al.*, 2009, 2014) and relevant features are summarised in the Supplementary Information.

We used thermogravimetry and differential scanning calorimetry (TGA-DSC) to quantify the abundances of serpentine and brucite, as well as the extents of serpentinisation. TGA-DSC is ideally suited for this purpose because dehydroxylation of serpentine and brucite involves mass loss and heat flow anomalies over distinct temperatures intervals (Lafay *et al.*, 2012; Okamoto *et al.*, 2011; Viti, 2010). Raman spectroscopy was performed for non-destructive, high resolution identification of minerals. Major element compositions of whole rock samples were determined by X-ray fluorescence. A description of the analytical techniques used is provided in the Supplementary

1. Woods Hole Oceanographic Institution, 266 Woods Hole Rd, Woods Hole, MA 02543, USA
2. Department of Geosciences and MARUM, University of Bremen, Klagenfurter Str., 28359 Bremen, Germany
* Corresponding author (email: fklein@whoi.edu)

Information. To assess the stabilities of minerals in the system MgO-SiO_2-H_2O, equilibrium constants for their dissolution were calculated using SUPCRT92 (Johnson *et al.*, 1992).

Results

TGA-DSC of serpentinites recovered by seafloor drilling and dredging yielded contrasting results (Figs. 1, S-1). With five exceptions (samples # 173-1068A-22R-1W 30-33 cm, 153-920B-1W-3W 64-66 cm, 153-920B-2R-1W 80-82 cm, 153-920B-10R-1W, 82-86 cm, 153-920B-10R-2W 68–70 cm), drilled serpentinites exhibited significant mass loss between 250 and 450 °C with a maximum between 315 and 380 °C accompanied by a marked endothermic heat flow anomaly. The mass loss and heat flow anomaly over this temperature interval are characteristic for dehydroxylation of Fe-bearing brucite (Okamoto *et al.*, 2011), which was also identified by means of Raman spectroscopy on the basis of diagnostic Raman bands at 279 cm^{-1}, 444 cm^{-1}, and 3650 cm^{-1} in pseudomorphic textures after olivine (Fig. 2). The identification of brucite is corroborated by previously published electron microprobe analysis of the same samples (Klein *et al.*, 2009, 2014). The mass loss from brucite due to the removal of water from its crystal structure was 1.24 to 4.60 wt. % (average of 2.61 wt. %). Considering that the approximate composition of brucite was $Mg_{0.8}Fe_{0.2}(OH)_2$ (Klein *et al.*, 2009, 2014) the measured mass loss suggests brucite contents of 3.56 to 15.61 wt. % (average of 8.58 wt. %). Twenty two of the drilled samples (n = 48) exhibited additional mass loss around 280 °C, which we attributed to dehydroxylation of the layered double hydroxide iowaite ($Mg_6Fe_2Cl_2(OH)_{16}$). The presence of iowaite was also indicated by Raman spectroscopy based on a strong Raman band at 527 cm^{-1}. Hyperspectral Raman maps suggested that iowaite occurs in mesh texture where it replaces brucite (Fig. 2). To assess the total amount of brucite formed during serpentinisation, we included any mass loss from dehydroxylation of minor iowaite (*i.e.* >250 °C) to brucite. This is justified because the molar ratio of (Mg + Fe)/OH in brucite and iowaite is 0.5, and iowaite formed at the expense of brucite likely without significantly changing its Mg/Fe ratio.

In contrast to drilled serpentinites, dredged serpentinites showed much smaller mass loss between 250 and 450 °C and no discernible heat flow anomaly over this temperature interval (Figs. 1, S-1, Table S-1). Hence, these samples do not contain brucite or iowaite in detectable amounts, *i.e.* they contain less than 0.4 wt. % brucite. A marked mass loss between 450 and 750 °C in conjunction with pronounced endothermic heat flow anomalies are diagnostic of dehydroxylation of serpentine in drilled and dredged serpentinites (Viti, 2010). Raman spectroscopy suggested that most samples are dominated by lizardite with additional chrysotile. However, samples from the Mariana

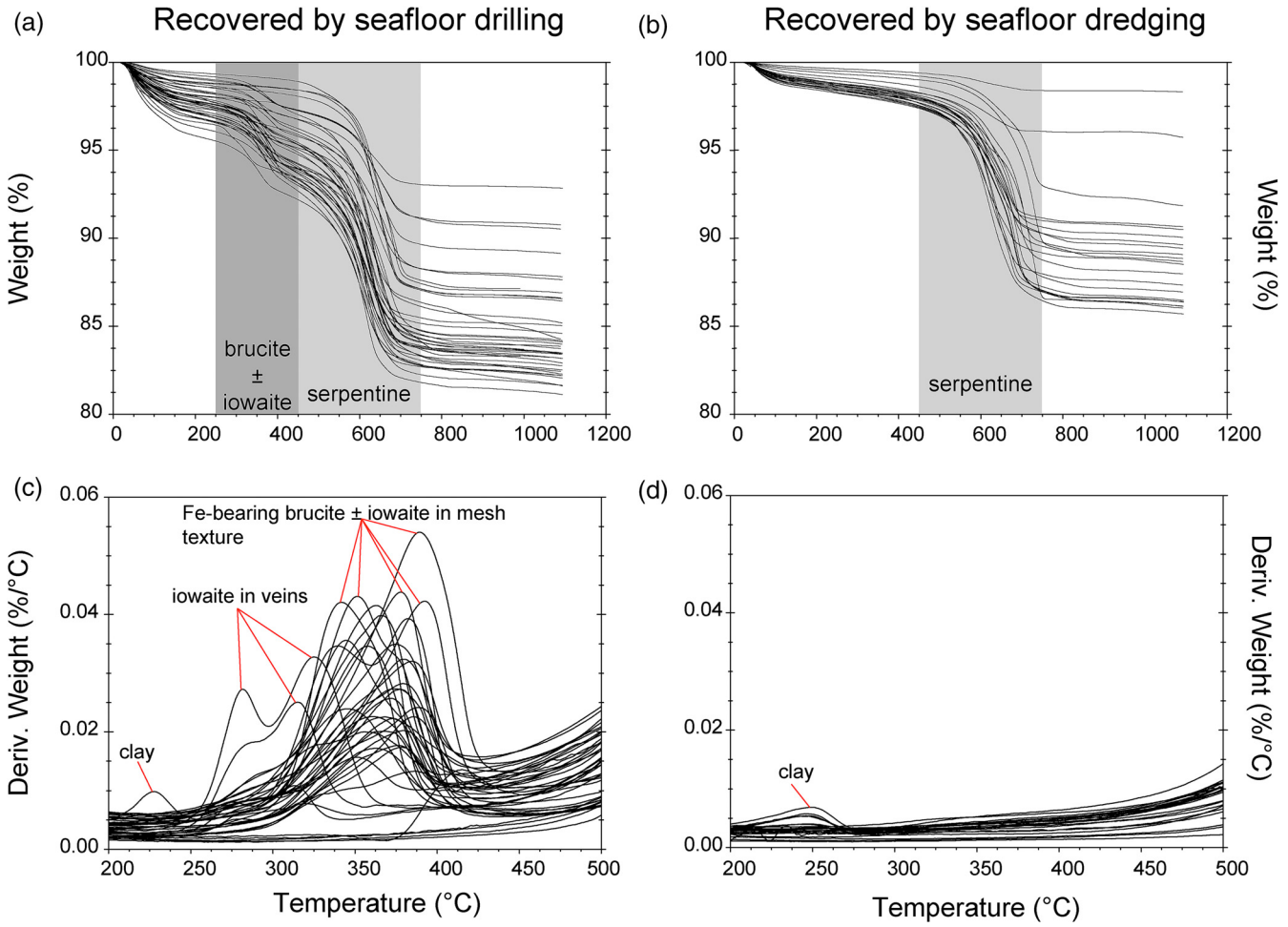

Figure 1 Thermal analysis of drilled **(a, c)** and dredged **(b, d)** serpentinites. Upper panels show the decrease in sample mass with temperature. Shading indicates mass loss *via* dehydroxylation of brucite ± iowaite (dark grey) and serpentine (grey). Lower panels show first derivative (deriv.) of mass loss between 200 and 500 °C. Dehydroxylation of brucite(±iowaite) is apparent in drilled samples but not in dredged samples.

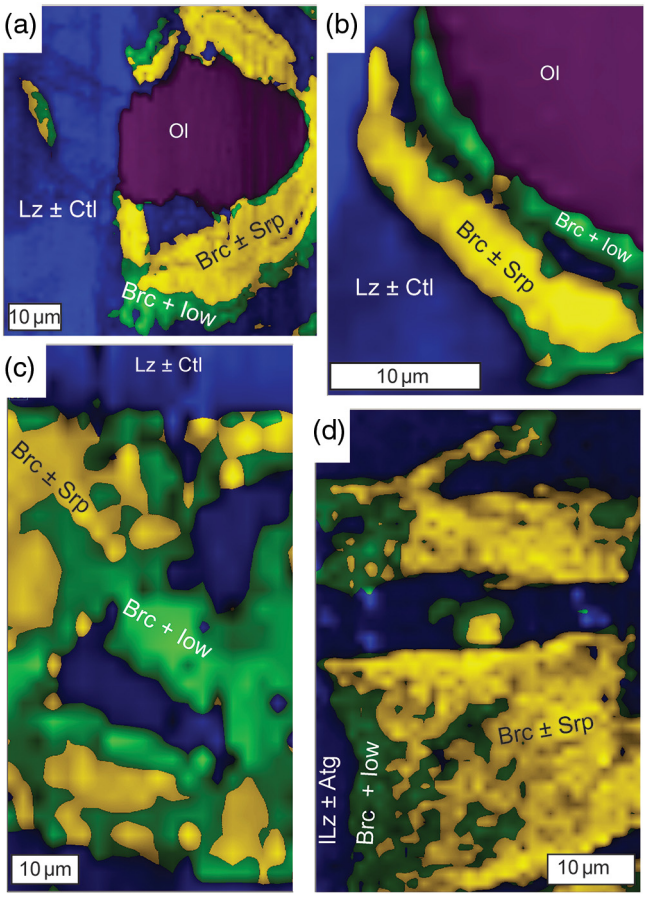

Figure 2 Hyperspectral Raman maps of brucite and serpentine in mesh texture in drilled samples. Some of the brucite is replaced by iowaite. Brucite and iowaite are intergrown with minor amounts of serpentine. **(a)** Sample 895D-3R-1W 64-66 cm. **(b)** Sample 1274A-3R1 111-120 cm. **(c)** Sample 1068A-24R-2W 56-59 cm. **(d)** 779A-03R-1W, 26–28 cm.

forearc (ODP Leg 125) also contained antigorite, which was reflected by slightly higher dehydroxylation temperatures when compared with lizardite and chrysotile. The mass loss attributed to the removal of water from the crystal structure of serpentine was 4.24 to 11.64 wt. % (average of 9.8 wt. %) in drilled samples, consistent with incomplete serpentinisation and the presence of brucite in these samples. Together, serpentine and brucite in partially to completely serpentinised peridotite examined here contain 5.88 to 14.19 wt. % water (average of 12.22 wt. %). Of the total water content in unweathered serpentinite, on average, 80.28 % is hosted by serpentine and 19.71 % by brucite. In dredged samples, mass loss attributable to water removal from serpentine was 1.0 to 11.2 wt. % (average of 8.1 wt. %). Here, any mass loss lower than the expected ~12.5 wt. % for pure serpentine is chiefly due to incomplete serpentinisation. Additional mass loss at temperatures lower than 250 °C is related to removal of adsorbed water, destabilisation of clay minerals, or loss of interlayer water molecules in iowaite (Fig. 1).

Discussion

Brucite formation during serpentinisation. Brucite is present in 90 % of the drilled serpentinites we examined (Figs. 1, S-1, Table S-1). It occurs together with serpentine in mesh texture and veins suggesting it formed at the expense of olivine under static conditions (Fig. 2). While brucite contents of serpentinites are variable, they increase with increasing whole rock water contents and with increasing whole rock Mg/Si ratios (Fig. 3). Since drilled samples examined in this study show no evidence of extensive Si metasomatism (Fig. S-2), our results point to protolith composition and the extent of alteration as the primary controls on brucite contents in serpentinised peridotites. Previous studies using closed system thermodynamic equilibrium models predicted the effect of the protolith olivine/pyroxene ratio on the abundance of brucite in serpentinite (Klein *et al.*, 2009, 2013; Malvoisin, 2015). Models for serpentinisation of pure olivine ($Mg_{1.8}Fe_{0.2}SiO_4$) by heated seawater predicted brucite contents ranging from 16.3 to 17.4 wt. % (or 46 to 49 mole %) between 250 and 150 °C, respectively, *i.e.* the temperature interval where much of seafloor serpentinisation takes place (Klein *et al.*, 2013, 2014). For comparison, complete serpentinisation of dunite produced 15.6 wt. % brucite (Fig. 3, Table S-1). With increasing

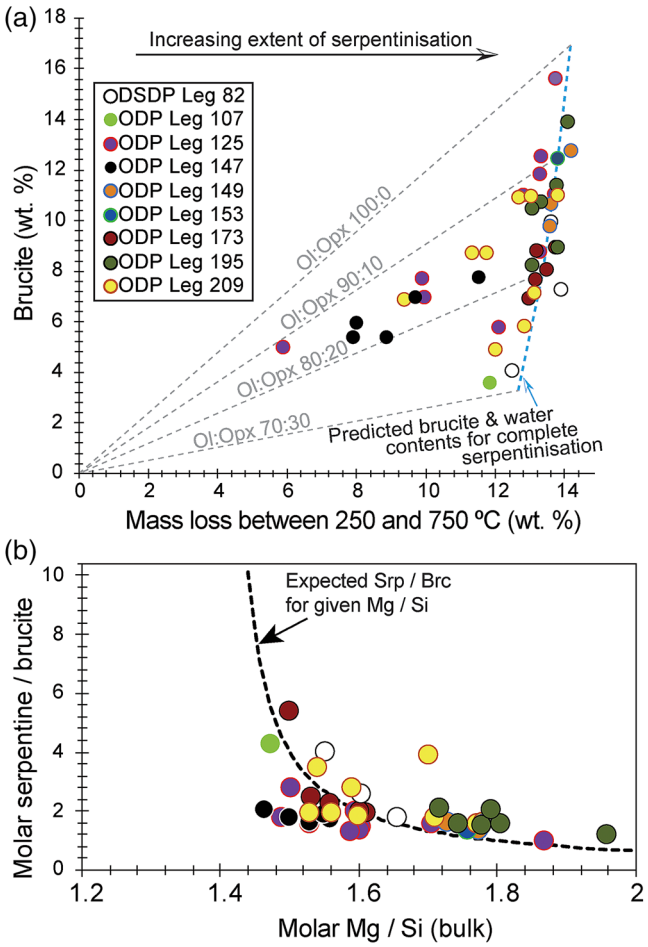

Figure 3 **(a)** Calculated brucite contents as a function of water content in serpentinite as derived from thermal analysis in comparison to brucite and water contents for serpentinisation of rocks with distinct modal proportions of olivine and orthopyroxene predicted from thermodynamic models (Klein *et al.*, 2013). Note that the trajectories (grey dashed lines) point to averages of predicted brucite contents for complete serpentinisation (blue dashed line) of ultramafic rocks between 250 and 150 °C. They do not imply that the amounts of brucite increase linearly with the extent of serpentinisation. **(b)** Molar serpentine/brucite ratios in serpentinite as a function of molar Mg/Si ratios of whole rock samples. Molar serpentine/brucite ratios derived from thermal analysis are close to expected ratios for given molar Mg/Si ratios (dashed line) suggesting Mg and Si was conserved during serpentinisation. Only samples that showed evidence for brucite from thermal analysis are included.

orthopyroxene content of the protolith, the modelled brucite contents for serpentinisation decreased due to the overall decreased Mg/Si ratios. Harzburgite with 20 vol. % orthopyroxene was predicted to yield 7.6 to 8.2 wt. % brucite (or 26 to 28 mole %) between 250 and 150 °C, while serpentinisation of harzburgite with 30 vol. % orthopyroxene would yield 3.0 to 3.5 wt. % (12 to 14 mole %) brucite over the same temperature range (Klein *et al.*, 2013). Drilled serpentinites contained 3.56 wt. % (or 14 mole %) brucite or more, and 8.58 wt. % (29 mole %) on average. If serpentinisation was quasi-isochemical with respect to Mg, Fe, and Si, their protoliths would have contained approximately 30 vol. % orthopyroxene or less and 20 vol. % orthopyroxene on average. Independent estimates from point counting of serpentinised abyssal peridotite (Michael and Bonatti, 1985; Dick, 1989; Snow and Dick, 1995; Ohara *et al.*, 2002) corroborate this estimate with an average orthopyroxene content of 20.8 vol. %. In general, therefore, the range in brucite contents of fully serpentinised peridotites that were recovered by seafloor drilling (Figs. 1, 3) can be explained by variations of the initial olivine/orthopyroxene ratio of the peridotite protolith.

Brucite dissolution during weathering. None of the dredged serpentinites examined here contain brucite or iowaite (Figs. 1, S-1). The lack of these minerals may be due to the addition of Si during serpentinisation. However, this would require that dredged serpentinite is affected by Si metasomatism whereas drilled serpentinite is not, an unlikely scenario. It has long been established that seawater is undersaturated with respect to brucite (Fig. 4; Nesbitt and Bricker, 1978). Consequently, serpentinites exposed to seawater on the seafloor for periods of time sufficient for low temperature weathering to occur are free of brucite – as our study demonstrates.

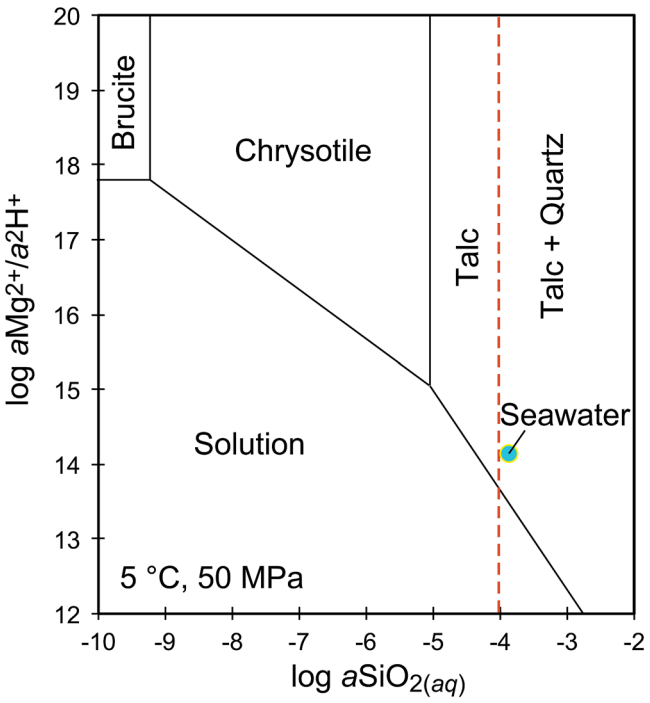

Figure 4 Activity-activity diagram depicting the stability fields of phases in the system MgO-SiO_2-H_2O at 5 °C and 50 MPa. Brucite is stable only at low activities (*a*) of H^+ (i.e. high pH) and $SiO_{2(aq)}$, and grossly undersaturated in seawater. The red dashed line indicates the solubility of quartz. For simplicity, only Mg end members are illustrated and the water activity is assumed to be unity. Equilibrium constants were calculated using SUPCRT92 (Johnson *et al.*, 1992).

While drilled serpentinites examined in this study do contain brucite, it is conceivable that seafloor weathering penetrates deeper into the subseafloor and dissolves brucite as the plate matures. In serpentinised dunite from ODP Site 1271 south of the 15° 20′ N Fracture Zone on the Mid-Atlantic Ridge, brucite is missing in the topmost core sections, but is abundant (10–15 vol. %) in serpentinite from >10 m sub-seafloor depth (Bach *et al.*, 2004). The basement at Site 1271 was exposed about 1.5 Ma (Bach *et al.*, 2011), suggesting that the brucite dissolution front propagated downward at a rate of <10 m *per* Myr. If we assume that 5 % (Carlson, 2001) of the seafloor in the Arctic, Atlantic, and Indian Oceans consists of serpentinite (~8,562,550 km^2), and that weathering leads to quantitative dissolution of brucite in the uppermost 100 m (*i.e.* in 856,255 km^3) with a 4.0 wt. % MgO loss on average (assuming serpentinite contains 8.58 wt. % brucite), we calculate a MgO mass of $\sim 9 \times 10^{19}$ g transferred from the lithosphere to the ocean since the breakup of Pangaea, *circa* 175 million years ago. This would translate to an average flux of MgO of $\sim 5 \times 10^{11}$ g/yr ($\sim 1 \times 10^{10}$ mol/yr). An upper estimate, where the seafloor of oceanic lithosphere accreted at slow and ultra-slow spreading ridges contains 25 % serpentinite and the depth of weathering is 200 m would result in an average annual MgO flux of $\sim 5 \times 10^{12}$ g/yr ($\sim 1 \times 10^{11}$ mol/yr). These fluxes are significant, but noticeably smaller than the continental runoff flux of 5×10^{12} mol/yr (*e.g.*, Spencer and Hardie, 1990). With an approximate composition of $Mg_{0.8}Fe_{0.2}(OH)_2$, the potential loss of FeO from dissolution of brucite is 1.8 wt. % on average. Much of this Fe may get oxidised and remain within the rock as ferric (oxyhydr)oxide alongside carbonate (Jöns *et al.*, 2017; Templeton and Ellison, 2020). Each mole of brucite that dissolves adds two moles of alkalinity to the oceans, which will facilitate the sequestration of CO_2 in the seabed. Complete oxidation and precipitation of Fe^{2+}, which is also released when brucite dissolves, will add 0.4 moles H^+ *per* mole $Mg_{0.8}Fe_{0.2}(OH)_2$, so the net alkalinity production *per* mole brucite dissolving is 1.6 moles. Hence, a net alkalinity flux on the order of 10^{11} mol/yr can be expected. The related CO_2 sink flux should be of similar magnitude, which is small (but perhaps not insignificant) compared to an annual oceanic outgassing flux of 2×10^{12} mole CO_2 (Marty and Tolstikhin, 1998).

Conclusions

Brucite in oceanic unweathered serpentinite recovered by drilling is common and widespread. This is at odds with the notion that oceanic serpentinite is brucite-poor, which resulted from a sampling bias toward dredged rocks that had undergone weathering. Brucite dissolution during weathering releases Mg; however, the resulting fluxes are small compared with the riverine input. If brucite dissolution in old ultramafic basement reached as deep as 200 m, then as much as 5 % of the CO_2 outgassing at mid-ocean ridges could be compensated by the related enhancement of alkalinity. Iron released *via* brucite dissolution is rapidly oxidised and largely conserved within the rock. Dissolution of olivine is an additional source of Mg and alkalinity to the oceans, but it is uncertain how much of that released flux is consumed by reverse weathering reactions.

The average brucite contents of unweathered serpentinites are close to those predicted from simple thermodynamic equilibrium models assuming primary mineral abundances characteristic of typical oceanic peridotite. Hence, the brucite contents of serpentinite examined in this study can be entirely explained by variations in the olivine/orthopyroxene ratio of the peridotite protolith. This finding also suggests that Mg, Fe, and Si are largely conserved during serpentinisation. The abundance of brucite determined here underscores the previously

suggested importance of brucite in affecting $aH_{2(aq)}$, $aSiO_{2(aq)}$, and the pH of oceanic serpentinisation systems. Notably, brucite hosts approximately 20 % of the water in unweathered serpentinite and, therefore, likely represents an important carrier of water into subduction zones.

Acknowledgements

We greatly appreciate constructive comments by B. Tutolo and an anonymous reviewer, as well as editorial handling by S. Opfergelt. Support for this project was provided by the Independent Research & Development Program at Woods Hole Oceanographic Institution, the US National Science Foundation (NSF Award # 1059534 and 9986135), and the Special Priority Program 1144 of the German Science Foundation (BA 1605/1-1 and BA 1605/1-2). This research would not have been possible without samples supplied by the Ocean Drilling Program and the Seafloor Samples Laboratory at WHOI.

Editor: Sophie Opfergelt

Additional Information

Supplementary Information accompanies this letter at https://www.geochemicalperspectivesletters.org/article2035.

Cite this letter as: Klein, F., Humphris, S.E., Bach, W. (2020) Brucite formation and dissolution in oceanic serpentinite. *Geochem. Persp. Let.* 16, 1–5.

References

Bach, W., Garrido, C.J., Harvey, J., Paulick, H., Rosner, M. (2004) Seawater-peridotite interactions – First insights from ODP Leg 209, MAR 15°N. *Geochemistry, Geophysics, Geosystems* 5, Q09F26, doi: 10.1029/2004GC000744.

Bach, W., Rosner, M., Jöns, N., Rausch, S., Robinson, L.F., Paulick, H., Erzinger, J. (2011) Carbonate veins trace seawater circulation during exhumation and uplift of mantle rock: Results from ODP Leg 209. *Earth and Planetary Science Letters* 311, 242–252.

Carlson, R.L. (2001) The abundance of ultramafic rocks in Atlantic Ocean crust. *Geophysical Journal International* 144, 37–48.

Dick, H.J.B. (1989) Abyssal peridotites, very slow spreading ridges and ocean ridge magmatism. In: Saunders, A.D., Norry, M.J. (Eds) *Magmatism in the Ocean Basins*. Blackwell, Oxford, 71–105.

Hostetler, P.B., Coleman, R.G., Mumpton, F.A., Evans, B.W. (1966) Brucite in alpine serpentinites. *American Mineralogist* 51, 75–98.

Johnson, J.W., Oelkers, E.H., Helgeson, H.C. (1992) SUPCRT92: A software package for calculating the standard molal thermodynamic properties of minerals, gases, aqueous species, and reactions from 1-5000 bars and 0-1000 °C. *Computers & Geosciences* 18, 899–947.

Jöns, N., Kahl, W.-A., Bach, W. (2017) Reaction-induced porosity and onset of low-temperature carbonation in abyssal peridotites: Insights from 3D high-resolution microtomography. *Lithos* 268–271, 274–284.

Kawahara, H., Endo, S., Wallis, S.R., Nagaya, T., Mori, H., Asahara, Y. (2016) Brucite as an important phase of the shallow mantle wedge: Evidence from the Shiraga unit of the Sanbagawa subduction zone, SW Japan. *Lithos* 254–255, 53–66.

Klein, F., Bach, W., Jöns, N., McCollom, T., Moskowitz, B., Berquó, T. (2009) Iron partitioning and hydrogen generation during serpentinization of abyssal peridotites from 15°N on the Mid-Atlantic Ridge. *Geochimica et Cosmochimica Acta* 73, 6868–6893.

Klein, F., Bach, W., McCollom, T.M. (2013) Compositional controls on hydrogen generation during serpentinization of ultramafic rocks. *Lithos* 178, 55–69.

Klein, F., Bach, W., Humphris, S.E., Kahl, W.-A., Jöns, N., Moskowitz, B., Berquó, T.S. (2014) Magnetite in seafloor serpentinite – Some like it hot. *Geology* 42, 135–138.

Lafay, R., Montes-Hernandez, G., Janots, E., Chiriac, R., Findling, N., Toche, F. (2012) Mineral replacement rate of olivine by chrysotile and brucite under high alkaline conditions. *Journal of Crystal Growth* 347, 62–72.

Malvoisin, B. (2015) Mass transfer in the oceanic lithosphere: Serpentinization is not isochemical. *Earth and Planetary Science Letters* 430, 75–85.

Marty, B., Tolstikhin, I.N. (1998) CO_2 fluxes from mid-ocean ridges, arcs and plumes. *Chemical Geology* 145, 233–248.

Michael, P.J., Bonatti, E. (1985) Peridotite composition from the North Atlantic: regional and tectonic variations and implications for partial melting. *Earth and Planetary Science Letters* 73, 91–104.

Nesbitt, H.W., Bricker, O.P. (1978) Low temperature alteration processes affecting ultramafic bodies. *Geochimica et Cosmochimica Acta* 42, 403–409.

Ohara, Y., Stern, R.J., Ishii, T., Yurimoto, H., Yamazaki, T. (2002) Peridotites from the Mariana Trough: first look at the mantle beneath an active back-arc basin. *Contributions to Mineralogy and Petrology* 143, 1–18.

Okamoto, A., Ogasawara, Y., Ogawa, Y., Tsuchiya, N. (2011) Progress of hydration reactions in olivine-H_2O and orthopyroxenite-H_2O systems at 250 °C and vapor-saturated pressure. *Chemical Geology* 289, 245–255.

Peters, D., Pettke, T., John, T., Scambelluri, M. (2020) The role of brucite in water and element cycling during serpentinite subduction – Insights from Erro Tobbio (Liguria, Italy). *Lithos* 360–361, 105431.

Snow, J.E., Dick, H.J.B. (1995) Pervasive magnesium loss by marine weathering of peridotite. *Geochimica et Cosmochimica Acta* 59, 4219–4235.

Spencer, R.J., Hardie, L.A. (1990) Control of seawater composition by mixing of river waters and mid-ocean ridge hydrothermal brines. In: Spencer, R.J., Chou, I.-M. (Eds). *Fluid-Mineral Interactions: A Tribute to H.P. Eugster*. The Geochemical Society, Special Publication No. 2, 409–419.

Templeton, A.S., Ellison, E.T. (2020) Formation and loss of metastable brucite: does Fe(II)-bearing brucite support microbial activity in serpentinizing ecosystems? *Philosophical Transactions of the Royal Society A: Mathematical, Physical and Engineering Sciences* 378, 20180423.

Viti, C. (2010) Serpentine minerals discrimination by thermal analysis. *American Mineralogist* 95, 631–638.

Geochemical Perspectives Letters

Brucite formation and dissolution in oceanic serpentinite

F. Klein, S.E. Humphris, W. Bach

Supplementary Information

The Supplementary Information includes:

- Analytical Methods
- Rock Description
- Figures S-1 and S-2
- Tables S-1 and S-2
- Supplementary Information References

Analytical Methods

Raman spectroscopy was conducted at Woods Hole Oceanographic Institution using a Horiba LabRam HR system equipped with 3 lasers (473 nm, 532 nm, 633 nm), two gratings (600, 1800 grooves per mm), and an Olympus BX41 microscope. The instrument was calibrated using the 520.7 cm^{-1} band of Si before each session and checked for drift every two hours. Most analyses were carried out using the 633 nm laser between 100 and 1280 cm^{-1}. To unequivocally distinguish serpentine minerals, additional analyses were conducted between 3500 and 3800 cm^{-1}. Spectra were processed with the Labspec 6 software suite for background subtraction and compared with reference spectra (Downs, 2006; Petriglieri *et al.*, 2015) for mineral identification.

A TA Instruments Q600 simultaneous thermal analyser was used at Woods Hole Oceanographic Institution for differential scanning calorimetry and thermogravimetric analysis to determine the presence and amounts of brucite and serpentine. We adopted this approach from previous studies that successfully used thermogravimetry to determine the abundances of serpentine and brucite formed during hydrothermal laboratory experiments (Okamoto *et al.*, 2011; Lafay *et al.*, 2012). The mass loss due to dehydroxylation of brucite, i.e. $Mg(OH)_2 \rightarrow MgO + H_2O$ is proportional to the abundance of brucite in a sample. Likewise, the mass loss due to dehydroxylation of serpentine ($Mg_3Si_2O_5(OH)_4$) is

proportional to the abundance of serpentine in a sample. While dehydroxylation of serpentine is complete at 750°C, its decomposition involves a series of reaction products including talc ($Mg_3Si_4O_{10}(OH)_2$ and forsterite (Mg_2SiO_4); *i.e.*, $5Mg_3Si_2O_5(OH)_4 \rightarrow Mg_3Si_4O_{10}(OH)_2 + 6Mg_2SiO_4 + 9H_2O$, and, in a second step, talc reacts with forsterite to form enstatite ($MgSiO_3$); *i.e.*, $Mg_3Si_4O_{10}(OH)_2 + Mg_2SiO_4 \rightarrow 5MgSiO_3 + H_2O$ (Gualtieri *et al.*, 2012). As shown in Figure 1, the dehydroxylation of brucite and serpentine take place over discrete temperature intervals, which can be conveniently used to determine their abundances. Any mass loss between 250 and 450°C was attributed to dehydroxylation of brucite, whereas any mass loss between 450 and 750°C was attributed to dehydroxylation of serpentine (Fig. 1). Molar proportions and concentrations of serpentine and brucite of individual samples were calculated by assuming that the molar X_{Mg} (Mg/(Mg+Fe)) of brucite was 0.8 and that of serpentine was 0.95, with molar masses of 64.63 g/mol and 281.84 g/mol, respectively. This assumption is simplistic considering the Fe contents of these minerals are variable; however, such variations have a negligible effect on calculated molar serpentine / brucite ratios. Except for the dehydroxylation of iowaite, which forms at the expense of brucite without modifying its (Mg+Fe)/OH ratio, no other minerals underwent dehydroxylation between 250 and 450 °C. Chlorite, which commonly occurs as an accessory mineral in bastite texture, would show characteristic dehydroxylation patterns between 460 and 865 °C (Földvári, 2011) that were not observed in our measurements. Hence, the possible presence of trace amounts of chlorite did not affect the interpretation of our data to any significant extent.

For each analysis, 20-50 mg of finely powdered material was heated from room temperature to 1100°C (heating rate = 10°C per minute) in a N_2 atmosphere (flow rate = 50 mL per minute). Repeated measurements of standard materials supplied by the manufacturer suggest that the temperature is accurate to 1°C and the weight change to 0.5 µg. Brucite-free serpentinite showed an average baseline weight loss of 0.9% between 250 and 450°C, which was subtracted from the measured values over this temperature interval for calculation of brucite contents. Based on repeat analyses, the limit of quantification for mass loss of water from hydrous minerals was better than 0.1 wt.%, which would correspond to 0.4 wt. % brucite with the composition $Mg_{0.8}Fe_{0.2}(OH)_2$.

Major elements of dredged samples were analysed using X-ray fluorescence (XRF) at the Peter Hooper GeoAnalytical Lab at the Washington State University (Pullman, WA) (Johnson *et al.*, 1999). Loss on ignition (LOI) was also measured at the GeoAnalytical Lab by heating the dredged samples in ceramic crucibles to 900 °C. Major element data of drilled samples examined in this study are taken from Klein *et al*. (2017).

Equilibrium constants for dissolution of minerals displayed in Figure 4 were calculated using the modelling code SUPCRT92 (Johnson *et al.*, 1992) using a customised database that contains thermodynamic data of minerals and aqueous species. Details of this database are provided elsewhere (Klein *et al.*, 2009, 2013).

Rock Description

Protoliths of serpentinites included mostly harzburgite and dunite. The extent of serpentinisation ranged from incipient in peridotite mylonite to complete in protogranular peridotite. Serpentinisation involved the formation of the serpentine group minerals lizardite and chrysotile, as well as antigorite in samples from the Mariana forearc. Magnetite is more abundant in samples from mid-ocean ridges that formed at relatively high temperatures than in samples from passive margins and subduction zone forearcs. Talc and chlorite are accessories in bastite texture of some serpentinites from mid-ocean-ridge settings; however, we did not include samples that underwent extensive talc-alteration in this study. The occurrence of brucite was previously established in select samples that were recovered by seafloor drilling using electron microprobe analysis and confocal Raman spectroscopy (Klein *et al.*, 2009, 2014; Kahl *et al.*, 2015; Nielsen *et al.*, 2015). Evidence for several serpentinisation events was commonly expressed through cross-cutting veins of distinct generations in all samples. Some of the dredged samples showed visible signs of weathering, such as orange-red staining and weathering rinds. To examine differences in weathering extent, samples from the weathering rind (halo) and the sample interior were analysed (sample IO11-76 60 171a & IO11-76 60 171b). Some of the dredged samples showed visible evidence for extensive to pervasive weathering (K162-9 30-105, CHN35 7-92, VULC-5 41-29, OCE-23 14-1. AII107-6 40-31) whereas others did not appear to be weathered (K162-9 45-25, K162-9 58-33, CHN35 7-383, CHN35 7-15, CHN35 18-109, CHN35 18-287, IO11-76 60-27, IO11-76 60-60, IO11-76 60-165, VULC-5 41-13, OCE-23 14-3, AII107-6 40-46). However, TGA-DSC revealed that all of the dredged samples had undergone weathering, even the seemingly unweathered ones.

Supplementary Figures

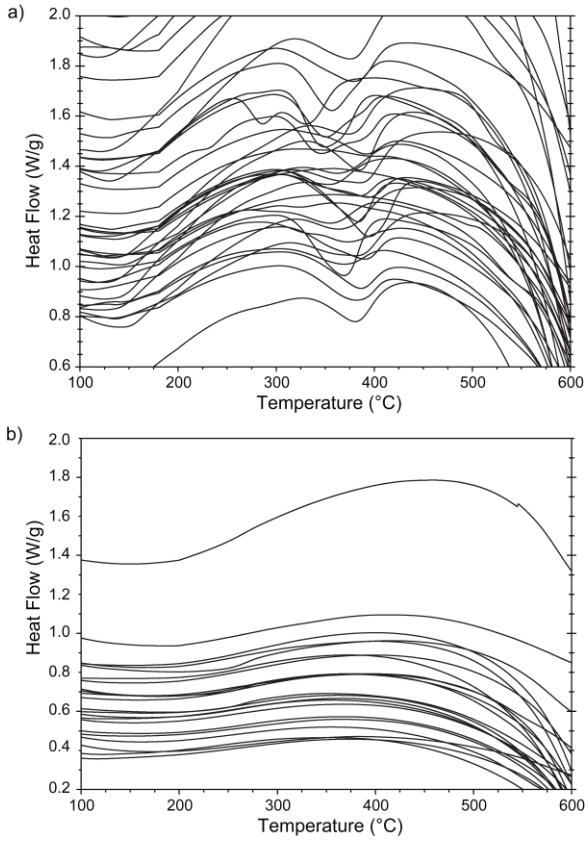

Figure S-1 Differential scanning calorimetry of drilled **(a)** and dredged **(b)** serpentinites. Drilled serpentinites show a pronounced negative (endothermic) heat flow anomaly between 300 and 400 °C attributed to Fe-bearing brucite. In contrast, dredged serpentinites do not show an endothermic heat flow anomaly, indicating that these samples do not contain brucite.

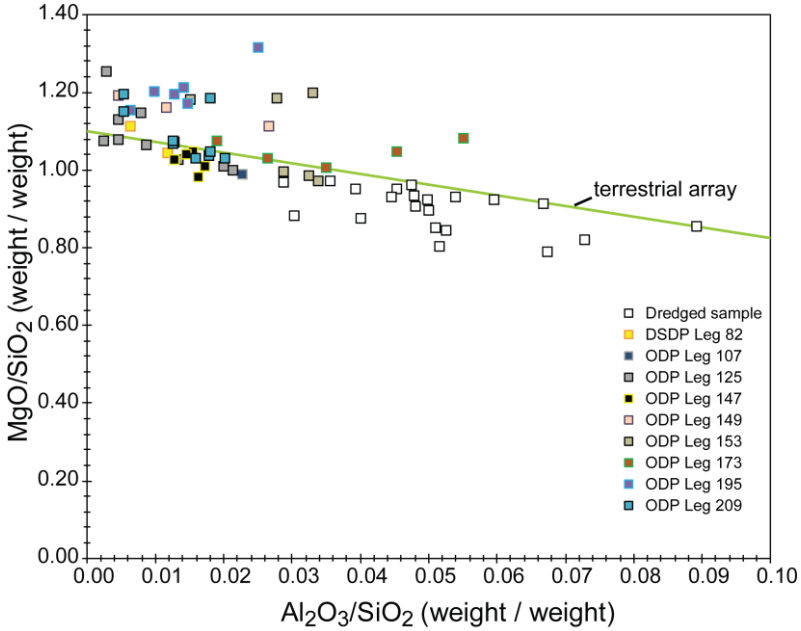

Figure S-2 Major element ratios of samples examined in this study. The terrestrial array (Hart and Zindler, 1986; Jagoutz *et al.*, 1979) is shown for comparison. Drilled samples scatter around the terrestrial array whereas dredged samples fall below it. The decreased MgO/SiO_2 of dredged samples is attributed to loss of Mg. The addition of Si would shift both MgO/SiO_2 and Al_2O_3/SiO_2 to lower values; however, such a trend is not evident. Whole rock major element data of serpentinised peridotites recovered by seafloor drilling are taken from previous studies of the same samples (Paulick *et al.*, 2006; Klein *et al.*, 2017).

Supplementary Tables

Table S-1 Summary of thermogravimetric analysis and molar Mg/Si.

Sample ID	*Area*	*Meters below seafloor [$] (drilled samples)*	*Weight loss (%) 250-450 °C*	*Weight loss (%) 450-750 °C*	*Brucite** (wt.%)*	*MgO from brucite (wt.%)*	*molar Srp/Brc ratio*	*Molar Mg/Si of whole rock**	**Primary DTG peak at temperature (˚C)**	**Secondary DTG peak**
Drilled Samples										
082-558Z-42R-1W, 9-11	Azores, off axis	130.09	1.38	11.11	4.06	2.03	4.03	1.55	313	276
082-558Z-42R-1W, 133-135	Azores, off axis	131.33	2.27	11.64	7.25	3.62	2.56	1.60	325	280
082-558Z-43R-1W, 45-46	Azores, off axis	139.45	3.02	10.59	9.94	4.96	1.75	1.66	315	284
107-651A-57R-2W, 140-142	Tyrrhenian Sea	146.40	1.24	10.62	3.56	1.78	4.28	1.47	276	319
125-779A-03R-1W, 26-28	Conical Seamount	10.86	3.33	10.38	11.06	5.52	1.56	1.71	357	shoulder
125-779A-05R-2W, 35-38	Conical Seamount	31.40	3.31	9.52	10.98	5.48	1.44	1.60	374	shoulder
125-779A-08R-1W, 45-47	Conical Seamount	58.95	2.40	7.51	7.72	3.85	1.56	1.53	388	shoulder
125-779A-10R-2W, 51-53	Conical Seamount	79.44	3.54	9.74	11.81	5.89	1.38	1.60	392	-
125-779A-13R-2W, 46-48	Conical Seamount	108.56	2.19	7.79	6.97	3.48	1.78	1.49	385	-
125-779A-17R-4W, 32-34	Conical Seamount	149.94	1.64	4.24	4.99	2.49	1.29	1.59	378	-
125-779A-25R-1W, 88.5-91	Conical Seamount	197.69	4.60	9.16	15.61	7.79	1.00	1.87	389	-
125-779A-26R-2W, 72-74	Conical Seamount	208.16	1.85	10.27	5.75	2.87	2.78	1.50	384	shoulder
125-779A-33R-2W, 80-82	Conical Seamount	275.32	2.68	10.61	8.73	4.36	1.98	1.59	344	shoulder
125-779A-35R-1W, 22-24	Conical Seamount	293.52	3.74	9.60	12.53	6.25	1.28	1.68	365	-
147-895D-2R-1W, 29-31	Hess Deep	16.29	1.75	7.11	5.39	2.69	2.03	1.46	362	-
147-895D-3R-1W, 64-66	Hess Deep	26.64	2.19	7.53	6.97	3.48	1.72	1.56	377	-
147-895D-4R-3W, 114-116	Hess Deep	38.13	1.90	6.10	5.93	2.96	1.61	1.53	379	-
147-895D-5R-1W, 121-123	Hess Deep	44.51	1.75	6.15	5.39	2.69	1.76	1.50	375	-
147-895D-7R-3W, 13-15	Hess Deep	67.66	2.41	9.12	7.76	3.87	1.89	1.55	371	-
149-897D-23R-1W, 17-20	Iberian Margin	115.37	2.97	10.63	9.76	4.87	1.79	1.65	365	shoulder
149-897D-23R-2W, 63-64	Iberian Margin	117.13	3.80	10.39	12.74	6.36	1.37	1.77	351	shoulder
149-897D-24R-3W, 103-106	Iberian Margin	127.95	3.21	10.41	10.63	5.30	1.62	1.73	344	shoulder
153-920B-1W-3W, 64-66	MARK	3.12	0.49	10.95	-	-	-	1.48	-	-
153-920B-2R-1W, 80-82	MARK	14.80	0.35	10.99	-	-	-	1.47	-	-
153-920B-10R-1W, 82-86	MARK	89.92	0.39	11.37	-	-	-	1.78	-	-
153-920B-10R-2W, 68-70	MARK	91.14	0.53	11.12	-	-	-	1.45	-	-
153-920B-12R-2W, 140-143	MARK	110.55	3.72	10.08	12.46	6.21	1.35	1.76	382.00	334

Table S-1 cont.

Sample ID	*Area*	*Meters below seafloor [$] (drilled samples)*	*Weight loss (%) 250-450 °C*	*Weight loss (%) 450-750 °C*	*Brucite** (wt.%)*	*MgO from brucite (wt.%)*	*molar Srp/Brc ratio*	*Molar Mg/Si of whole rock**	Primary DTG peak at temperature (˚C)	Secondary DTG peak
173-1068A-22R-1W, 30-33	Iberian Margin	3.67	0.99	10.67	-	-	-	1.50	-	
173-1068A-24R-1W, 73-74	Iberian Margin	32.80	2.50	11.00	8.07	4.03	2.20	NA	372.00	shoulder
173-1068A-24R-2W, 56-59	Iberian Margin	33.84	2.70	10.49	8.80	4.39	1.94	1.61	377.00	shoulder
173-1068A-25R-1W, 104-106	Iberian Margin	42.54	2.38	10.79	7.65	3.82	2.27	1.56	363.00	shoulder
173-1068A-26R-1W, 14-16	Iberian Margin	46.01	2.74	11.01	8.94	4.46	2.01	1.60	355.00	shoulder
173-1068A-28R-1W, 49-50	Iberian Margin	55.76	2.17	10.79	6.89	3.44	2.49	1.53	350.00	shoulder
195-1200A-11R-1W, 47-49	South Chamorro	89.87	3.42	10.35	11.37	5.67	1.51	1.78	384.00	shoulder
195-1200A-13R-1W, 121-124	South Chamorro	109.91	3.24	10.08	10.72	5.35	1.56	1.80	379.00	-
195-1200A-16R-2W, 48-50	South Chamorro	139.43	2.73	11.08	8.91	4.45	2.03	1.79	360.00	-
195-1200A-7R-2W, 127-129	South Chamorro	52.96	4.12	9.99	13.89	6.93	1.21	1.96	378.00	-
195-1200A-3R-1W, 3-7	South Chamorro	18.23	2.54	10.55	8.21	4.10	2.08	1.72	373.00	-
195-1200A-17G-2W, 76-79	South Chamorro	unknown	3.17	9.92	10.46	5.22	1.57	1.74	379.00	shoulder
209-1271A_4R2_5-15	MAR 15°20 FZ	29.75	3.04	9.66	10.02	5.00	1.59	1.77	363.00	-
209-1271B_17R1_61-69	MAR 15°20 FZ	85.11	3.05	9.98	10.05	5.01	1.64	1.78	341.00	shoulder
209-1272A_14R1_43-53	MAR 15°20 FZ	66.13	1.62	11.22	4.92	2.46	3.46	1.54	332.00	282
209-1272A_21R1_88-100	MAR 15°20 FZ	99.78	1.99	11.13	6.25	3.12	2.80	1.59	325.00	282
209-1272A_27R2_78-88	MAR 15°20 FZ	129.28	2.43	9.32	7.83	3.91	1.92	1.56	322.00	280
209-1274A_6R3_24-34	MAR 15°20 FZ	33.06	1.91	7.48	5.96	2.97	1.96	1.53	383.00	shoulder
209-1274A_16R2_26-38	MAR 15°20 FZ	85.40	3.06	10.75	10.09	5.03	1.76	1.71	338.00	shoulder
209-1274A_24R1_16-26	MAR 15°20 FZ	131.96	1.36	10.66	3.99	1.99	3.92	1.70	316.00	-
209-1274A_27R1_130-140	MAR 15°20 FZ	147.40	2.43	8.92	7.83	3.91	1.84	1.60	346.00	shoulder
Dredged samples										
K162-9 30-105	SWIR, Oblique SC		0.84	8.28	-	-	-	1.21	-	-
K162-9 45-25	SWIR, Oblique SC		1.03	11.22	-	-	-	1.43	-	-
K162-9 58-23	SWIR, Oblique SC		0.53	7.61	-	-	-	1.17	-	-
K162-9 58-33	SWIR, Oblique SC		0.83	10.15	-	-	-	1.35	-	-
CHN35 7-15	MAR St. Paul's Rocks		0.54	2.54	-	-	-	1.39	-	-
CHN35 7-92	MAR St. Paul's Rocks		0.69	7.84	-	-	-	1.38	-	-
CHN35 7-383	MAR St. Paul's Rocks		0.25	1.00	-	-	-	1.42	-	-

Table S-1 cont.

Sample ID	*Area*	*Meters below seafloor $ (drilled samples)*	*Weight loss (%) 250-450 °C*	*Weight loss (%) 450-750 °C*	*Brucite** (wt.%)*	*MgO from brucite (wt.%)*	*molar Srp/Brc ratio*	*Molar Mg/Si of whole rock**	Primary DTG peak at temperature (˚C)	Secondary DTG peak
CHN35 18-109	MAR St. Paul's Rocks		0.30	6.21	-	-	-	1.27	-	-
CHN35 18-287	MAR St. Paul's Rocks		0.35	9.15	-	-	-	1.36	-	-
IO11-76 60-27	SWIR Islas Orcadas FZ		0.74	9.20	-	-	-	1.37	-	-
IO11-76 60-51	SWIR Islas Orcadas FZ		0.81	7.42	-	-	-	1.19	-	-
IO11-76 60-60	SWIR Islas Orcadas FZ		0.87	10.68	-	-	-	1.42	-	-
IO11-76 60-165	SWIR Islas Orcadas FZ		0.88	10.54	-	-	-	1.38	-	-
IO11-76 60-171a	SWIR Islas Orcadas FZ		0.75	11.08	-	-	-	1.44	-	-
IO11-76 60-171b	SWIR Islas Orcadas FZ		0.91	10.30	-	-	-	1.39	-	-
VULC-5 35-37	SAAR Bullard FZ		0.68	7.63	-	-	-	1.30	-	-
VULC-5 41-13	SAAR Bullard FZ		1.03	7.88	-	-	-	1.22	-	-
VULC-5 41-29	SAAR Bullard FZ		0.67	6.96	-	-	-	1.27	-	-
OCE-23 14-1	Mid-Cayman Rise		0.80	6.89	-	-	-	1.26	-	-
OCE-23 14-3	Mid-Cayman Rise		0.56	8.48	-	-	-	1.33	-	-
AII107-6 40-31	SWIR Bouvet FZ		0.87	8.56	-	-	-	1.31	-	-
AII107-6 40-46	SWIR Bouvet FZ		0.71	10.90	-	-	-	1.44	-	-

$ refers to igneous basement not counting sediments, ** reported brucite contents include minor iowaite recalculated as brucite, * molar ratio of whole rocks from X-ray fluorescence, wt.% = weight percent, DTG = 1st derivative of weight loss, NA = not analysed, MARK = Mid-Atlantic Ridge Kane fracture zone area, MAR = Mid-Atlantic Ridge, FZ = fracture zone, SWIR = Southwest Indian Ridge, SC = spreading center, SAAR = South American Antarctic Ridge

Table S-2 X-ray fluorescence analysis of major elements in dredged samples.

Sample #	SiO_2 wt. %	Al_2O_3 wt. %	TiO_2 wt. %	FeO wt. %	MnO wt. %	CaO wt. %	MgO wt. %	K_2O wt. %	Na_2O wt. %	P_2O_5 wt. %	Total wt. %	Loss on Ignition wt. %
K162-9 30-105	46.88	2.93	0.056	8.91	0.135	2.07	38.07	0.04	0.37	0.022	99.49	11.50
K162-9 30-106	46.37	1.11	0.015	9.65	0.146	0.54	41.43	0.03	0.32	0.043	99.66	14.46
K162-9 45-25	45.73	2.18	0.028	8.20	0.117	0.05	43.85	0.02	0.15	0.004	100.33	14.53
K162-9 58-23	46.40	3.13	0.082	10.51	0.188	2.30	36.57	0.03	0.35	0.027	99.59	11.20
K162-9 58-33	46.18	2.22	0.052	7.94	0.146	0.37	41.83	0.03	0.23	0.005	99.00	13.27
CHN35 7-92	44.30	2.39	0.068	8.10	0.160	2.47	41.19	0.10	0.45	0.029	99.26	3.96
CHN35 7-92	41.14	2.46	0.050	8.32	0.168	8.42	37.98	0.07	0.44	0.058	99.11	9.94
CHN35 7-383	44.46	2.02	0.033	9.40	0.195	0.92	42.21	0.03	0.14	0.005	99.41	1.11
CHN35 18-109	44.88	4.01	0.255	7.84	0.117	3.71	38.33	0.18	0.48	0.019	99.83	7.58
CHN35 18-287	44.15	2.95	0.223	8.69	0.127	2.80	40.27	0.15	0.24	0.062	99.66	11.04
IO11-76 60-27	46.03	2.32	0.024	7.84	0.137	0.67	42.35	0.02	0.14	0.000	99.53	11.99
IO11-76 60-51	47.56	2.46	0.029	8.89	0.128	2.35	38.11	0.06	0.32	0.011	99.92	10.32
IO11-76 60-60	45.86	1.81	0.020	8.27	0.125	0.11	43.58	0.03	0.16	0.006	99.98	13.94
IO11-76 60-165	46.42	2.07	0.020	8.37	0.121	0.21	43.06	0.02	0.19	0.005	100.49	13.85
IO11-76 60-171a	44.88	1.60	0.031	9.13	0.096	0.11	43.48	0.03	0.19	0.012	99.56	13.72
IO11-76 60-171B	46.11	2.21	0.020	8.30	0.131	0.40	42.95	0.03	0.25	0.007	100.40	13.60
VULC-5 35-37	46.58	1.87	0.020	8.78	0.118	1.85	40.70	0.04	0.19	0.008	100.15	9.97
VULC-5 41-13	46.73	3.41	0.092	8.73	0.148	2.70	38.31	0.03	0.29	0.006	100.44	11.26
VULC-5 41-29	46.60	2.38	0.050	8.78	0.130	2.37	39.58	0.04	0.22	0.017	100.16	9.17
OCE-23 14-1	44.83	2.36	0.039	9.36	0.149	4.72	37.76	0.02	0.24	0.032	99.51	9.54
OCE-23 14-3	46.05	2.31	0.036	8.69	0.164	1.48	41.14	0.02	0.14	0.006	100.03	10.92
AII107-6 40-31	46.67	1.42	0.004	9.01	0.133	1.36	41.12	0.03	0.23	0.019	99.99	13.04
AII107-6 40-46	45.71	1.32	0.005	8.43	0.131	0.08	44.25	0.03	0.16	0.006	100.12	13.75
IO11-76 60-27*	45.86	2.28	0.023	8.41	0.135	0.64	42.44	0.02	0.12	0.000	99.93	12.01
CHN35 7-92*	41.04	2.44	0.049	8.57	0.167	8.42	37.87	0.06	0.41	0.058	99.08	9.98
IO11-76 60-27**	45.72	2.28	0.025	8.43	0.135	0.65	41.97	0.02	0.14	0.000	99.37	11.97

* duplicates, **triplicates

Table S-2 cont.

Element oxides recalculated on a hydrous basis

Sample #	SiO_2 wt. %	Al_2O_3 wt. %	TiO_2 wt. %	FeO wt. %	MnO wt. %	CaO wt. %	MgO wt. %	K_2O wt. %	Na_2O wt. %	P_2O_5 wt. %	Total wt. %	
K162-9 30-105	**41.61**	2.61	0.05	7.89	0.12	1.84	33.84	0.04	0.33	0.02	88.35	
K162-9 45-25	40.19	1.92	0.02	7.21	0.10	0.04	38.54	0.02	0.13	0.00	88.17	
K162-9 58-23	42.43	2.86	0.07	9.61	0.17	2.10	33.44	0.03	0.32	0.02	91.06	
K162-9 58-33	40.93	1.97	0.05	7.04	0.13	0.33	37.07	0.03	0.20	0.00	87.74	
CHN35 7-15	42.63	2.30	0.07	7.80	0.15	2.38	39.64	0.10	0.43	0.03	95.52	
CHN35 7-92	36.98	2.21	0.04	7.60	0.15	7.58	34.13	0.06	0.38	0.05	89.19	
CHN35 7-383	43.78	1.99	0.03	9.26	0.19	0.91	41.57	0.03	0.14	0.00	97.90	
CHN35 18-109	41.57	3.71	0.24	7.27	0.11	3.44	35.50	0.17	0.44	0.02	92.47	
CHN35 18-287	39.33	2.63	0.20	7.74	0.11	2.49	35.87	0.13	0.21	0.06	88.78	
IO11-76 60-27	40.74	2.04	0.02	7.31	0.12	0.58	37.52	0.02	0.12	bd	88.46	
IO11-76 60-51	43.07	2.23	0.03	8.05	0.12	2.13	34.51	0.05	0.29	0.01	90.48	
IO11-76 60-60	39.99	1.58	0.02	7.22	0.11	0.10	38.01	0.03	0.14	0.01	87.19	
IO11-76 60-165	40.36	1.80	0.02	7.28	0.11	0.18	37.44	0.02	0.17	0.00	87.38	
IO11-76 60-171a	38.88	1.39	0.03	7.91	0.08	0.10	37.67	0.03	0.16	0.01	86.25	
IO11-76 60-171b	40.17	1.93	0.02	7.23	0.11	0.35	37.42	0.03	0.22	0.01	87.47	
VULC-5 35-37	42.16	1.69	0.02	7.94	0.11	1.67	36.84	0.04	0.17	0.01	90.64	
VULC-5 41-13	41.85	3.05	0.08	7.82	0.13	2.42	34.31	0.03	0.26	0.01	89.95	
VULC-5 41-29	42.51	2.17	0.04	7.96	0.12	2.17	36.21	0.04	0.21	0.02	91.45	
OCE-23 14-1	40.89	2.15	0.04	8.54	0.14	4.31	34.44	0.02	0.22	0.03	90.77	
OCE-23 14-3	41.03	2.06	0.03	7.74	0.15	1.32	36.65	0.02	0.12	0.01	89.12	
AII107-6 40-31	40.89	1.24	0.00	7.89	0.12	1.19	36.03	0.03	0.20	0.02	87.62	
AII107-6 40-46	39.91	1.15	0.00	7.36	0.11	0.07	38.64	0.03	0.14	0.01	87.42	

Supplementary Information References

Downs, R.T. (2006) The RRUFF Project: an integrated study of the chemistry, crystallography, Raman and infrared spectroscopy of minerals. Program and Abstracts of the 19th General Meeting of the International Mineralogical Association in Kobe, Japan. O03-13 2006.

Földvári, M. (2011) *Handbook of the thermogravimetric system of minerals and its use in geological practice*. Geological Institute of Hungary, Budapest.

Gualtieri, A.F., Giacobbe, C., Viti, C. (2012) The dehydroxylation of serpentine group minerals. *American Mineralogist* 97, 666–680.

Hart, S.R., Zindler, A. (1986) In search of a bulk-Earth composition. *Chemical Geology* 57, 247–267.

Jagoutz, E., Palme, H., Baddenhausen, H., Blum, K., Cendales, M., Dreibus, G., Spettel, B., Lorenz, V., Wanke, H. (1979) The abundances of major, minor and trace elements in the earth's mantle as derived from primitive ultramafic nodules. *Lunar and Planetary Inst.~Technical Report*, 610–612.

Johnson, D.M., Hooper, P.R., Conrey, R.M. (1999) XRF Analysis of Rocks and Minerals for Major and Trace Elements on a Single Low Dilution Li-tetraborate Fused Bead. *Advances in X-ray Analysis, v, 41, p. 843–867 Le Bas, M.J.*

Johnson, J.W., Oelkers, E.H., Helgeson, H.C. (1992) SUPCRT92: A software package for calculating the standard molal thermodynamic properties of minerals, gases, aqueous species, and reactions from 1-5000 bars and 0-1000°C. *Computers & Geosciences* 18, 899–947.

Kahl, W.-A., Jöns, N., Bach, W., Klein, F., Alt, J.C. (2015) Ultramafic clasts from the South Chamorro serpentine mud volcano reveal a polyphase serpentinization history of the Mariana forearc mantle. *Lithos* 227, 1–20.

Klein, F., Bach, W., Jöns, N., McCollom, T., Moskowitz, B., Berquó, T. (2009) Iron partitioning and hydrogen generation during serpentinization of abyssal peridotites from 15°N on the Mid-Atlantic Ridge. *Geochimica et Cosmochimica Acta* 73, 6868–6893.

Klein, F., Bach, W., McCollom, T.M. (2013) Compositional controls on hydrogen generation during serpentinization of ultramafic rocks. *Lithos* 178, 55–69.

Klein, F., Bach, W., Humphris, S.E., Kahl, W.-A., Jöns, N., Moskowitz, B., Berquó, T.S. (2014) Magnetite in seafloor serpentinite - Some like it hot. *Geology* 42, 135–138.

Klein, F., Humphris, S.E., Marschall, H.R., Bowring, S.A., Horning, G. (2017) Mid-ocean ridge serpentinite in the Puerto Rico Trench: from seafloor spreading to subduction. *Journal of Petrology* 58, 1729–1754.

Lafay, R., Montes-Hernandez, G., Janots, E., Chiriac, R., Findling, N., Toche, F. (2012) Mineral replacement rate of olivine by chrysotile and brucite under high alkaline conditions. *Journal of Crystal Growth* 347, 62–72.

Nielsen, S.G., Klein, F., Kading, T., Blusztajn, J., Wickham, K. (2015) Thallium as a tracer of fluid-rock interaction in the shallow Mariana forearc. *Earth and Planetary Science Letters* 416–426.

Okamoto, A., Ogasawara, Y., Ogawa, Y., Tsuchiya, N. (2011) Progress of hydration reactions in olivine-H_2O and orthopyroxenite-H_2O systems at 250 °C and vapor-saturated pressure. *Chemical Geology* 289, 245–255.

Paulick, H., Bach, W., Godard, M., de Hoog, J.C.M., Suhr, G., Harvey, J. (2006) Geochemistry of abyssal peridotites (Mid-Atlantic Ridge, 15°20'N, ODP Leg 209): implications for fluid-rock interaction in slow spreading environments. *Chemical Geology* 234, 179–210.

Petriglieri, J.R., Salvioli-Mariani, E., Mantovani, L., Tribaudino, M., Lottici, P.P., Laporte-Magoni, C., Bersani, D. (2015) Micro-Raman mapping of the polymorphs of serpentine. *Journal of Raman Spectroscopy* 46, 953–958.